EQUIVALENCE RATIO EFFECTS IN TURBULENT, PREMIXED METHANE-AIR FLAMES

Marcus S. Day*, John B. Bell, Joseph F. Grcar and Michael J. Lijewski

Center for Computational Sciences and Engineering
Lawrence Berkeley National Laboratory
1 Cyclotron Road, Berkeley CA, 94720-8142 USA
web page: http://seesar.lbl.gov/ccse/
*e-mail: MSDay@lbl.gov

Key words: Direct numerical simulation, low Mach number, lean premixed turbulent methane flames

Abstract. *Turbulent methane flames exhibit a change in Markstein number as the equivalence ratio changes. In this paper, we demonstrate how these changes in Markstein number are related to shifts in the chemistry and transport. We focus on the analysis of simulations of two-dimensional premixed turbulent methane flames at equivalence ratios ϕ=0.55 and ϕ=1.00 computed using the GRI-Mech 3.0 mechanism. The simulations were performed using a low Mach number adaptive mesh refinement algorithm coupled to an automatic feedback control algorithm that stabilizes the flame on the computational grid. The flames are characterized in terms of curvature, strain and a local fuel-consumption-based flame speed. Joint probability density functions show correlations of the local flame speed with curvature and a lack of correlation with the tangential strain rate. We then introduce a pathline diagnostic that follows parcels of fluid through the flame, enabling us to quantify the associated reaction and diffusive transport processes. Using this diagnostic, we examine the differences in the chemical and transport properties of the two flames, and isolate those responsible for the shift in the correlation of local flame speed with flame surface curvature.*

1 INTRODUCTION

In classical premixed flame theory, the Markstein number relates the response of the flame (flame speed) to the stretching of the flame (for example, see Peters[1]), which includes components due to flow field strain and flame surface curvature. For premixed methane flames, experimental data[2] and simulations[3] show that the Markstein number depends on equivalence ratio and, in fact, changes sign as ϕ is reduced from stoichiometric conditions to lean conditions. Our goal in this paper is to relate these observations to specific chemical and transport processes in the flames. To facilitate this analysis, we introduce a diagnostic tool for analyzing multi-component, multi-dimensional reacting flow problems

with detailed kinetics. We assume that the analysis is performed in post-processing so that the distribution of all species as well as the temperature and velocity fields over all space and time are known. We note that although the analysis here is for 2D simulations the diagnostic approach is useful, and largely identical, for analysis of any multidimensional reacting flow problem.

Because of the relevance to existing and advanced commercial burners, we focus the analysis on flames in the corrugated/wrinkled laminar flamelet regime. We define this regime to be consistent with the map of turbulent combustion interaction regimes discussed at length in Peters.[1] In the corrugated/wrinkled laminar flamelet regime, the scales of the turbulent perturbations relative to those of the flame chemistry are such that velocity fluctuations modify the thermal profiles just upstream of the flame, yet have only moderate influence on the structure of the fundamental combustion reactions. Notwithstanding, the local rate of fuel consumption often scales with the flame geometry and flow perturbations upstream of the flame surface.

In an earlier paper,[4] we introduced an automatic control algorithm that can be used to stabilize a premixed turbulent flame in a simple idealized configuration. A flat steady laminar premixed flame is initialized in a computational domain and allowed to propagate toward an inlet boundary where turbulent perturbations have been superimposed on a mean inflow. A simple feedback control algorithm is employed to dynamically adjust the mean inflow rate at this boundary to stabilize the mean flame position in the domain. In this paper, we consider two premixed methane flames at different equivalence ratios in two dimensions, each of which have their position controlled using this algorithm. We examine in detail the statistics of local fuel consumption, flame surface curvature and flow field strain. Although the configurations are two dimensional, we will refer to the flames as turbulent. While the 2D approximation does not realistically represent turbulence, we nevertheless expect the results to be relevant to realistic conditions.[5,6] We use a new diagnostic algorithm to look in detail at the chemical and transport behavior of the flames, and quantify shifts in flame dynamics with changes in fuel equivalence ratio.

There is an extensive literature on computational studies of this type in 2D without feedback control, both with simplified and detailed chemistry and transport models. Examples include Baum et al.[7] who studied turbulent flame interactions for detailed hydrogen chemistry, and Haworth et al.[8] who examined the effect of inhomogeneous reactants for propane–air flames using detailed propane chemistry. Analogous studies in 3D have been performed by Rutland and Trouvé,[6] Trouvé and Poinsot,[9] Zhang and Rutland,[10] and Chakraborty and Cant.[11] All of these 3D studies were based on simplified chemistry. More recently, Tanahashi et al.[12,13] have performed 3D simulations of this type for turbulent premixed hydrogen flames with detailed hydrogen chemistry. Bell et al.[14] performed a similar study for a turbulent methane flame. None of the previous studies have focused on the interaction of preferential diffusion, turbulent flame surface fluctuations, and the detailed chemical response of the flames.

In the next section, we briefly discuss computational approach used to evolve the re-

acting flow problems. The following section then introduces the diagnostic procedure for interrogating the simulation data. The final section contains a detailed analysis of the simulated flames. First, we illustrate the large-scale structure of the flames and quantify how the flames respond to curvature and strain. Then we apply the new diagnostic algorithm to elucidate the mechanisms leading to the changes in flame response. In particular, we will show quantitatively how preferential diffusion and chemistry play different roles in lean and stoichiometric methane flames near curved regions of the flame surface.

2 COMPUTATIONAL MODEL

2.1 Reacting flow solver

The simulations we analyze here are based on a low Mach number formulation of the reacting Navier-Stokes equations, in which the background thermodynamic pressure remains constant. The methodology treats the fluid as a mixture of perfect gases, and uses a mixture-averaged model for differential species diffusion, ignoring Soret, Dufour and radiation effects. With these assumptions, the equations governing the flow are given by

$$\frac{\partial \rho U}{\partial t} + \nabla \cdot \rho U U \quad = \quad -\nabla \pi + \nabla \cdot \tau, \tag{1}$$

$$\frac{\partial \rho Y_m}{\partial t} + \nabla \cdot U \rho Y_m \quad = \quad \nabla \cdot \rho D_m \nabla Y_m + \rho \dot{\omega}_m, \tag{2}$$

$$\frac{\partial \rho h}{\partial t} + \nabla \cdot U \rho h \quad = \quad \nabla \cdot \frac{\lambda}{c_p} \nabla h + \sum_m \nabla \cdot h_m \Big(\rho D_m - \frac{\lambda}{c_p} \Big) \nabla Y_m, \tag{3}$$

where ρ is the density, U is the velocity, Y_m is the mass fraction of species m, h is the mass-weighted enthalpy of the gas mixture, T is the temperature, and $\dot{\omega}_m$ is the net creation rate for specie m due to chemical reactions. Also, λ is the thermal conductivity, τ is the stress tensor, c_p is the specific heat of the mixture, $h_m(T)$ and D_m are the enthalpy and species mixture-averaged diffusion coefficients of species m, respectively. These evolution equations are supplemented by an equation of state for the perfect gas mixture:

$$p_0 = \rho R_{mix} T = \rho \mathcal{R} T \sum_m \frac{Y_m}{W_m} \tag{4}$$

where W_m is the molecular weight of species m, $\mathcal{R}$ is the universal gas constant, and p_0 is the ambient (atmospheric) thermodynamic pressure. In the low Mach number model, the equation of state constrains the evolution of the system, and acoustic wave propagation is analytically removed from the dynamics of the system.

The basic discretization algorithm combines a symmetric operator-split treatment of chemistry and diffusion processes with a density-weighted approximate projection method for incorporating the velocity divergence constraint that enforces the equation of state constraint. This integration scheme is embedded in a parallel adaptive mesh refinement

(AMR) algorithm. The adaptive algorithm is second-order accurate in space and time, and discretely conserves species mass and enthalpy. No explicit model for turbulence or turbulence/chemistry interaction is included. The reader is referred to[15] for details of the low-Mach-number model and its numerical implementation and to[14, 16–18] for additional applications of this methodology to the simulation of premixed turbulent flames.

2.2 Computational setup

Two methane flames were simulated using the control formalism discussed above (and presented in detail in Bell et al.[4]) using the GRI-Mech 3.0 chemical mechanism, which contains 53 species, and 325 reactions. We consider inlet equivalence ratios of $\phi = 0.55$ and 1.0 to highlight variations observed in a methane flame's response to flowfield strain and flame surface curvature (see, for example, Tseng et al.[2]). Table 1 lists various properties of the corresponding steady laminar one-dimensional flame solutions computed using the PREMIX[19] code.

The flow configuration we consider initializes a flat laminar flame in a domain oriented so that the flame propagates downward. (Since there is no gravity in the present model, the coordinate directions are arbitrary). A cold fuel-air premixture enters the domain through bottom boundary, and hot combustion products exit the domain through the top. The remaining computational boundaries are periodic. The computational domains have dimensions $L \times H = 46 \, \delta_L \times 92 \, \delta_L$, where δ_L is the thermal thickness of the corresponding flat laminar flame. Along the inlet face we specify a mean inflow velocity and superimpose turbulent fluctuations The fluctuations in the inflow stream were generated for each case separately by generating a random vorticity field shaped spectrally to correspond to two-dimensional isotropic decaying turbulence. This random field is then evolved in time with an incompressible Navier Stokes solver to ensure proper phasing of the resulting velocity field. The resulting fluctuations have an effective integral scale length $\ell_t \sim 2.6\delta_L$ and turbulent intensity $u' \sim 1.7 s_L$, measured with respect to the properties of each flame. These scales are chosen arbitrarily so that both flames are in the corrugated/wrinkled laminar flamelet regime. The inlet face measures $L \approx 17.5\ell_t$ ensuring that the results are

Table 1: *Characteristics of the laminar methane-air flames of different stoichiometries at 1 atmosphere. Thermal flame thickness is calculated as the change in temperature through the flame divided by the maximum temperature gradient, $\delta_L = (T_{\max} - T_{\min})/\max \|\nabla T\|$.*

fuel equiv-alence ratio ϕ	thermal flame thickness δ_L (μm)	flame speed s_L (cm / s)	fuel consum-ption rate (g / cm s)	isotherm of peak heat release (K)	peak local fuel consumption (mg / mL s)
0.55	1313	7.62	0.0273	1379	7.03
1.00	433	36.2	0.2380	1684	134

insensitive to the width of the periodic domain.

Adaptive mesh refinement was used to maintain approximately 44 uniform grid cells across the thermal width of the flames throughout their evolution. Dynamic refinement for these simulations was based on the magnitude of vorticity and on a flame marker, CH_3. Prior to collecting data for analysis, both cases were evolved numerically until the mean flame location and mean inlet flow velocity became statistically stationary.

3 PATHLINE ANALYSIS

We want to be able to analyze in detail the transport and chemical properties of the simulated flames. Traditional flame analysis paradigms are based on instantaneous Eulerian snapshots of the solutions, and may employ local coordinates in a neighborhood of the instantaneous flame location. Here, we adopt a Lagrangian perspective in which we follow the fluid as it interacts with the flame. To make this notion precise, we identify an "infinitesimally small" parcel of the fluid and follow it as it passes into the flame zone, reacts and is then transported into the products. As we follow this parcel of fluid we can decompose the changes in its composition into two effects: changes due to reaction and changes due to transport. To express this mathematically, we write the species transport equations in Lagrangian form

$$\rho \frac{DY_m}{Dt} = \nabla \cdot \rho D_m \nabla Y_m + \rho \dot{\omega}_m, \tag{5}$$

This equation expresses the change in Y_m along integral curves in space and time of the velocity; i.e., curves given by

$$\frac{dx}{dt} = v(x, t) , \tag{6}$$

commonly referred to as pathlines. In the Lagrangian frame the continuity equation reduces to

$$\frac{D\rho}{Dt} = 0$$

so that, as the parcel of fluid is transported, the net mass in the parcel remains the same. The change in density along the pathline thus represents not a change in the mass of the parcel but rather a change in the volume that the parcel occupies.

Before discussing how to separate the diffusion and chemistry components of the pathline evolution, it is useful to consider the choice of units for the analysis. There are several possibilities that can be considered; here we have chosen to use $Y_m/W_m \equiv [X_m]/\rho$, which expresses the moles per unit mass in the parcel. This provides a natural way of representing the molar composition of the fluid parcel so that changes in the volume of the mixture do not change the representation. For example if there is no species transport or chemical reaction in the system then Y_m/W_m will remain unchanged along the pathline.

The basic idea is to follow selected pathlines in the flow that represent parcels of fluid, monitoring changes in composition of the parcel and the volume it occupies. The change

in composition can then be decomposed into the changes caused by reaction and those caused by species transport.

Although this type of analysis could be done while the simulation is in progress, that would impose fairly severe limitations on its utility. In particular, we would have to know *a priori* what initial parcels of fluid we want to follow. Looking at other locations would require repeating the simulation. Instead of trying to perform this analysis as part of the simulation, we use it as a post-processing tool.

Given a time sequence of snapshots of the evolving simulation, it is easy to construct a pathline passing through a selected feature in the solution by interpolating the velocity field from the simulations in space and time and integrating Eqn. 6 in time. A similar type of interpolation procedure allows us to extract the composition of the mixture along the pathline. For the analyses conducted here we have used bilinear interpolation in space and linear interpolation in time to construct both the velocity field and the mixture composition. We characterize the mixture in terms of its temperature and mole fractions; other quantities can be derived from these using standard thermodynamic operations. (Here, p is fixed as a consequence of the low Mach number model; in a more general case where the model includes acoustic waves, one additional thermodynamic variable is needed.)

The decomposition of the change in composition into reaction and transport components is somewhat more involved. If the simulation data is stored at a sufficiently fine temporal resolution, viz., at time increments in which the chemical kinetics can be accurately captured with simple single-step temporal integration strategies, then a straightforward evaluation of the rates along the path provides an adequate characterization of the reaction rates, and the diffusive transport can be obtained from conservation considerations. However, in our case with the larger time step allowed by the low Mach number model, the chemical kinetics are stiff on the time scale of the solution algorithm. (Chemistry is treated with a stiff ODE package in our simulation methodology.) Under these conditions, a simple evaluation of the chemical rates leads to an inaccurate separation of chemistry and transport along the pathline. This issue is exacerbated by our adaptive mesh refinement algorithm that incorporates subcycling in time so that fine grid regions are advanced at a finer time increments. As a result of subcycling, we only have data available at temporal increment associated with the coarsest grid. In the present case, with 5 levels of adaptively refined grids, this means that between successive coarse time steps that can be archived, the finest level grids have advanced 16 time steps.

To circumvent this difficulty, we observe that the chemistry within the parcel is completely local. The only interaction a given parcel has with the surrounding fluid is through diffusive transport. We can use this property to construct a simple inverse problem whose solution will provide a decomposition of the right hand side of Eqn. 5. In particular, given (ρ_1, T_1, Y_m^1) and (ρ_2, T_2, Y_m^2) at the beginning and end of a time interval $[t_1, t_2]$, respectively

we compute the diffusion flux divergence, $\mathcal{D}$ such that

$$\frac{DY_m}{Dt} = \rho\dot{\omega}_m + \frac{\mathcal{D}}{\rho}$$

with $Y_m(t_1) = Y_m^1$ and $Y_m(t_2) = Y_m^2$. For this construction, we discretize the path in small increments and assume that we can approximate $\mathcal{D}$ by a constant for each species on each interval. Furthermore, we assume that density and enthalpy vary linearly along each small segment of the path. This procedure assumes that we are sampling the data at a resolution on which the fluid dynamical behavior is smooth, although the chemical behavior may not be. Since the enthalpy is not changed by chemical reactions, we are able to separate the thermal behavior of the mixture into changes due to reaction and changes to due to transport of heat by thermal conduction and species diffusion.

4   RESULTS

Two 2D turbulent premixed methane flames were evolved numerically. The mean flow velocity of the inlet fuel stream was dynamically adjusted to control the mean location of the flame height in the domain. After the flame position was stabilized and the global flame speed has become statistically stationary, data from the simulation was written at each coarse-grid time step (corresponding to once every 16 fine-grid time steps). In addition to the temperature, two components of velocity and the chemical composition, the simulation accumulated the integrated fuel consumption over all subcycled time steps. We focus of the first part of our analysis on the dependence of the local rate of fuel consumption on flame surface curvature and flowfield strain.

Figure 1 depicts the local fuel consumption in the domain, and includes a magnification of a sub-region for each equivalence ratio. For the $\phi = 0.55$ flame the fuel consumption is enhanced in regions that are convex with respect to reactants and is reduced in cusps that are convex with respect to products. Here, a normalized curvature, $\kappa = \delta_L\nabla \cdot \hat{n}$ where $\hat{n}$ is the normal to the flame, and oriented so that positive curvature corresponds to the flame being convex with respect to reactants (having the local center of curvature in the products). The situation for the stoichiometric flame is reversed with stronger burning at the cusps. This dependence on equivalence ratio is in agreement with experimental and computational evidence for premixed methane flames at atmospheric pressure.[2,3,20]

Classical premixed flame theory predicts that the flame speed will be modified by stretch effects, which are a composition of flame curvature and tangential strain. Furthermore, the theory predicts that for small stretch, the relationship between local flame speed and strain is linear; suitably normalized, the constant of proportionality is the Markstein number. A normalized tangential strain rate, S, is given by

$$S = (\delta_L/s_L)\,\hat{\tau} \cdot \nabla U \cdot \hat{\tau}, \;\; \hat{\tau} \perp \hat{n},$$

Note that since the fluid expands as it moves through the preheat zone, the choice of where to evaluate the strain becomes an issue. If the flame is defined as the isotherm of peak
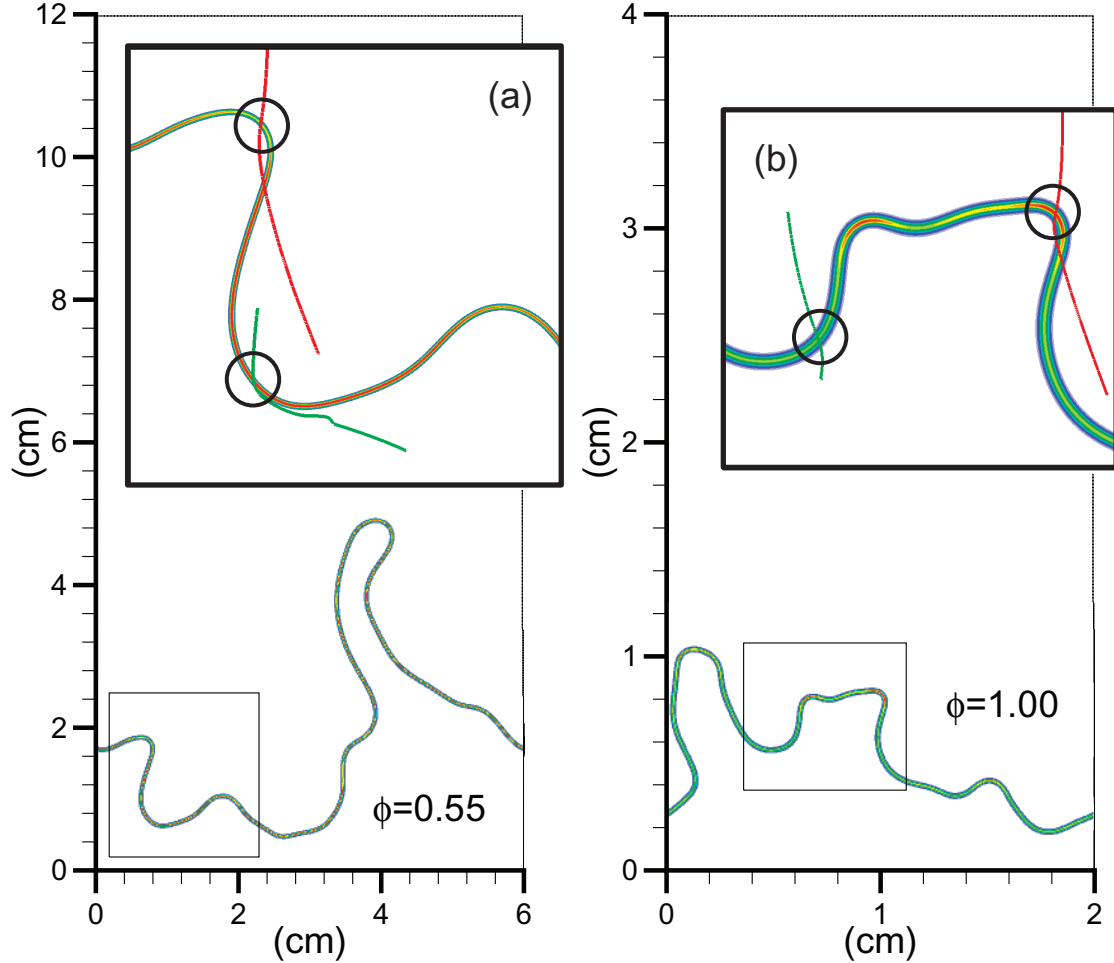
Figure 1: Detail of methane consumption rate for (a) $\phi = 0.55$, and (b) $\phi = 1.00$ in subregion near diagnostic pathlines, indicating opposite correlations with flame surface curvature. Green pathlines pass through the respective flame surface at the instant of this time snapshot through a "nose" region, red pathlines pass through "cusps".

fuel consumption, then expansion through the flame induces a strong correlation between curvature and strain as observed by Pope[21] and by Haworth and Poinsot.[22] An alternative, which we have adopted here, is to evaluate the strain at a relatively low temperature. In particular, we follow the integral curves of the progress variable until we reach the $T = 400\text{K}$ isotherm and evaluate the tangential strain rate there. This construction avoids flame acceleration effects but leads to other anomalies in highly cusped regions (discussed below). Probability density functions (PDF's) of the distribution of curvature and strain along the flame surface are shown in Fig. 2. Note that in these figures we have used a logarithmic vertical scale which accentuates low probability features. The
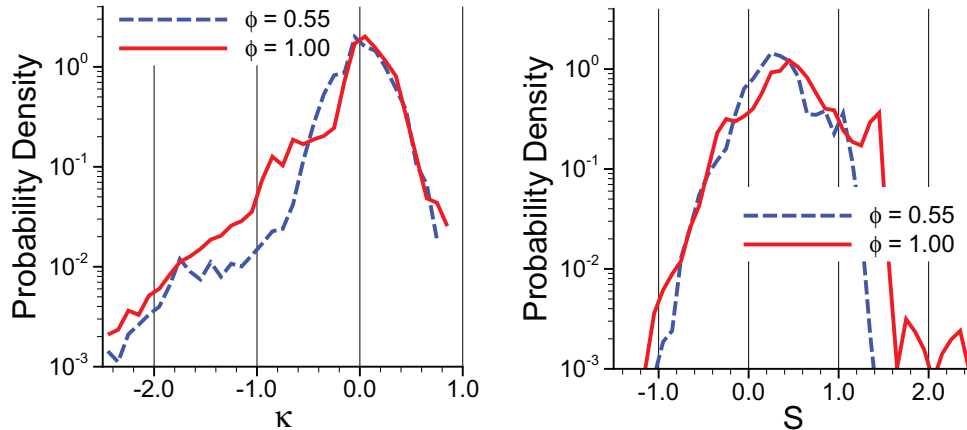
Figure 2: Probability density functions (PDF's) of nondimensionalized curvature and tangential strain of the flame sheet for the two cases considered. The flame sheet is defined to be the isotherm approximately coincident with peak heat release: 1379 and 1684 K, respectively. Strain is calculated on the cold side of the flame at the 400 K isotherm.

PDF of curvature shows a long low-probability tail at negative curvature. The peak of the strain rate PDF is positive indicating a slight bias toward extensive strain. Both of these characteristics are consistent with observations of other authors, such as Haworth and Poinsot.[22]

To quantify how curvature and strain affect the flame, we construct a local flame speed based on the consumption rate of methane. (There are several potential definitions of local flame speed; see, e.g., Poinsot and Veynante[23] for a discussion of possible choices.) We first identify the flame with the isotherm at which fuel consumption reaches its maximum in the corresponding flat unstretched laminar flame (Table 1). We then define a local coordinate system near the flame using the flame isotherm and a normal coordinate along ∇T. At uniform intervals along the flame, we follow integral curves of the ∇T toward both the products and fuel. These curves define a series of adjacent disjoint wedge-shaped volumes, Ω_k, surrounding the flame, and extend well beyond the region of high chemical reactivity. A normalized local burning speed may then be defined over each of these volumes:

$$S_c^{loc} = \frac{1}{A^{loc} \left(\rho Y_{\text{Fuel}} \right)_{\text{in}} s_L} \int_{\Omega_k} \rho \omega_{\text{Fuel}} d\Omega_k \qquad (7)$$

where A^{loc} is the length of the intersection of Ω_k with the flame. For additional detail about these constructions see Bell et al. [4]

Classical flame theory treats the flame as a discontinuous interface propagating through the fluid. Interpreting this theory in the context of resolved flames is problematic, particularly with respect to defining strain. (A number of authors have proposed thick flame modifications to the classical theory, see for example, Chung and Law[24] and de Goey

9

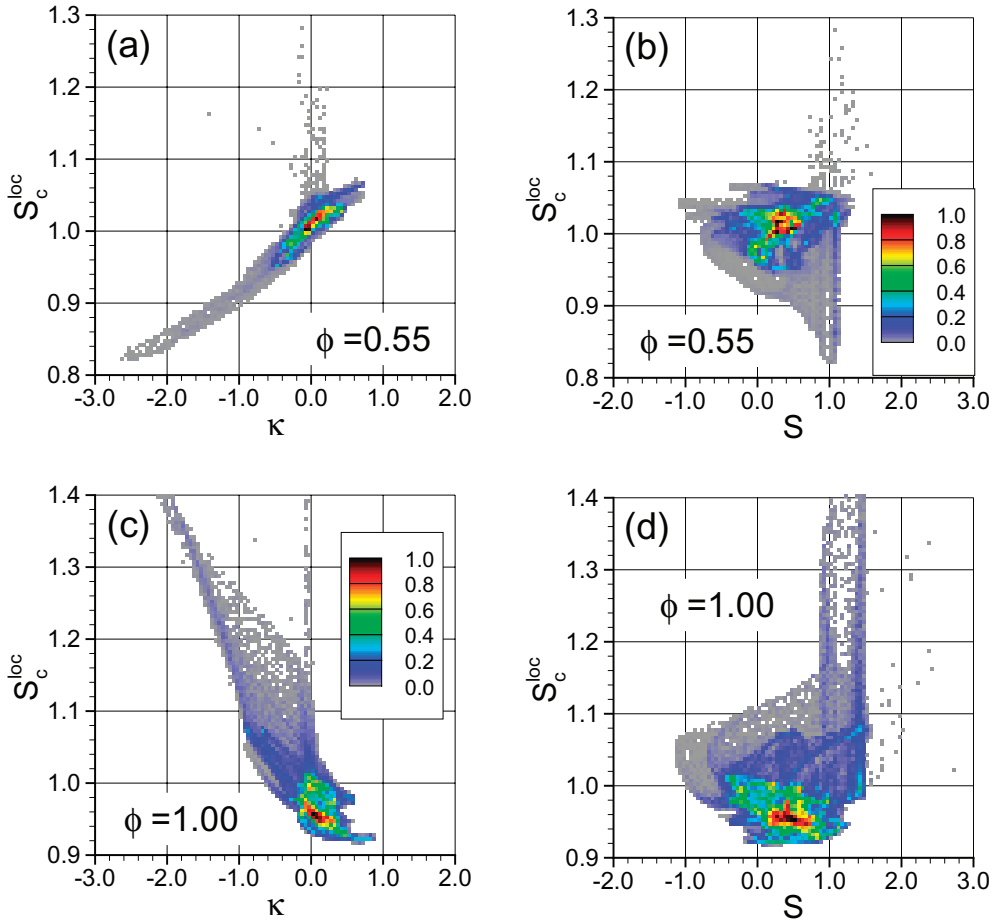and coworkers.[25–27]) In Fig. 3 we show joint PDFs of local consumption flame speed

Figure 3: Joint probability density functions (JPDF's) of three nondimensionalized quantities: fuel consumption speed, curvature, and tangential strain. The results for the $\phi = 0.55$ case are given in (a) and (b); the results for the $\phi = 1.00$ case are given in (c) and (d).
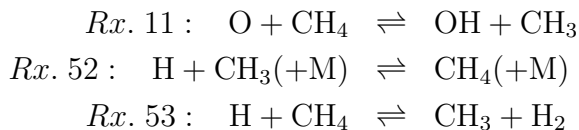
versus curvature and tangential strain. The data shows clear correlations between flame curvature the local rate of fuel consumption. For the $\phi = 0.55$ flame this correlation is positive with enhanced speeds in regions of positive curvature indicating that the flame is thermodiffusively unstable. For the $\phi = 1.00$ flame the situation is reversed with negative curvature regions burning most strongly. We note that some of the high local speeds near zero curvature represent a breakdown inherent in the construction of the integration regions Ω_k along integrals curves of ∇T. The high local speeds are associated with data from along flanks of long fingers of fuel that extend into the products. These regions also produce artifacts in the strain rate/flame speed joint PDF's that can be seen in Fig. 3b,d as vertical striations; in this case, the cold-strain evaluation location is anomalously

distant from the flame segment to which it is associated. The joint PDF of cold tangential strain rate and local flame speed shows essentially no correlation — indicating that, for these flames, the instantaneously evaluated tangential strain does not have a consistent local effect on the flame. A similar observation was made by Haworth and Poinsot[22] for single step chemistry. We note that with other definitions of strain we can obtain good correlations between local flame speed and tangential strain; however, we have found those correlations to be an artificial reflection of a strong correlation between tangential strain and curvature inside the flame zone.

As shown above, the correlation of local flame speed with curvature changes sign for the two equivalence ratios. We want to use pathline analysis to examine how differences in chemistry and transport between the two flames lead to these changes in flame response. To analyze this behavior, we construct two representative pathlines for each flame. In each case, one of the pathlines passes directly through a representative cusp and another passes through the flame in a region of positive curvature; we will refer to such a region as a "nose." The trajectories of the pathlines in space are superimposed on the magnified fuel consumption plots of Figure 1. We emphasize that the pathlines are curves in space-time, but to view them, we have drawn their entire spatial migration on top of the snapshot of the flame at the specific time that they cross the flame surface. Consequently, although it appears that the pathlines may cross the flame at an earlier time, this is simply an artifact of the picture; at the earlier time the flame was located elsewhere. We note that viewing the flame from the Lagrangian perspective of a fluid parcel passing through the flame is fairly complex. For comparison purposes, we construct pathlines for the corresponding flat laminar flames and focus the analysis on how the pathlines through noses and cusps differ from these.

In Fig. 4 (left) we show the temperature (K) and fuel (moles/g) of the fluid parcels for each pathline as a function of time. For these plots and the others in this section, we have shifted the time scale so that $t = 0$ corresponds to the time when that parcel of fluid crosses the isotherm of maximum fuel consumption. In both the lean and stoichiometric cases, the temperature and methane temporal profiles are considerably less steep at the noses than at the cusps, with the laminar flame being intermediate to the other two. Given the difference in the response of the two flames to curvature, this similarity is somewhat surprising. Naively, one might have expected that for the lean flame, the methane profiles would be reversed, reflecting the reduced burning intensity at cusps in that case. We also note that for both flames the temperature at peak fuel consumption is essentially the same at the cusps and noses.

Along the pathlines, there are four key reactions that play a dominant role in removing the first H atom from CH_4

$$Rx.\,11: \quad O + CH_4 \;\rightleftharpoons\; OH + CH_3$$
$$Rx.\,52: \quad H + CH_3(+M) \;\rightleftharpoons\; CH_4(+M)$$
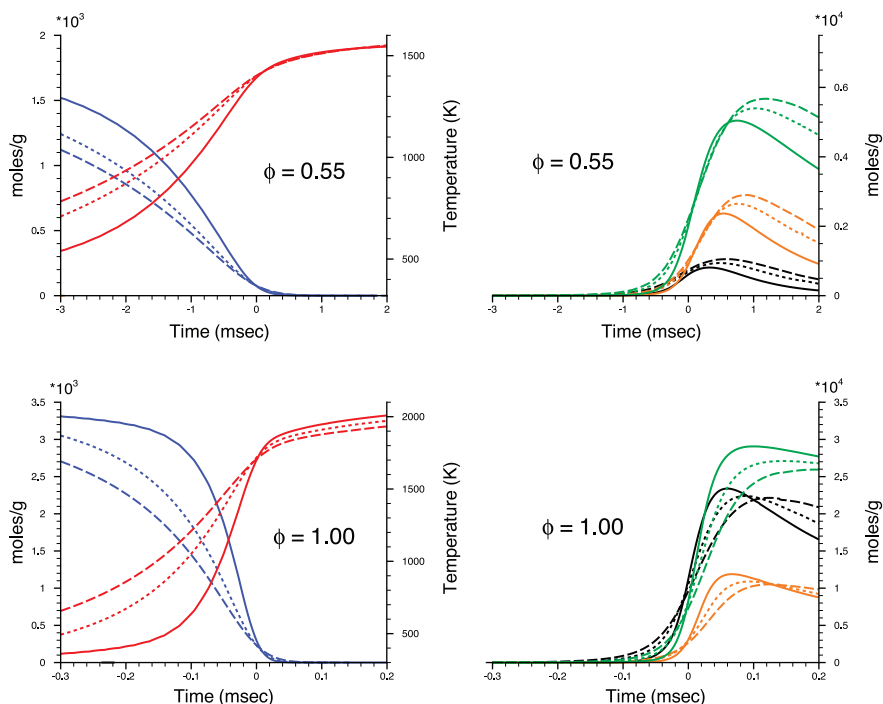$$Rx.\,53: \quad H + CH_4 \;\rightleftharpoons\; CH_3 + H_2$$

11

Figure 4: (left) Profiles of T (red) and CH_4 (blue) along the pathlines. Here the solid lines are the cusps, the long dashes are the noses and the short dashes are the laminar flame. (right) Profiles of radicals H (black), OH (green) and O (orange) along the pathlines. Again, the solid lines are the cusps, the long dashes are the noses and the short dashes are the laminar flame.

$$Rx.\,98: \quad OH + CH_4 \;\rightleftharpoons\; CH_3 + H_2O$$

(The reaction numbers correspond to the ordering in the GRI-3.0 reaction mechanism specification.) Thus, the radicals, H, O, and OH are the key reaction partners that control the destruction of CH_4. These three radicals are plotted in Fig. 4 (right), revealing some differences between the response of the two flames to the geometry of the flame surface. In both cases, the radical profiles peak after the methane has been consumed–the radicals are created downstream, after the fuel is consumed, and diffuse against the flow of fuel. For the rich flame, we see that the peak concentration of the radicals is higher in the cusp than in the nose. Also, the most prevalent radicals are OH and H; the O radical concentration is substantially smaller than the other two. For the lean flame, we note two major departures from these observations. First, the higher peak concentration for each radical occurs in the nose not the cusp. In addition, although OH remains the most plentiful radical, the concentration of H is now substantially reduced while the relative amount of O has increased.

The effect of these differences on the reaction profiles is shown in Figure 5. Here we plot the net reaction rate for each of the reactions mentioned above as a function of time for each flame, with the convention that positive values refer to the production of
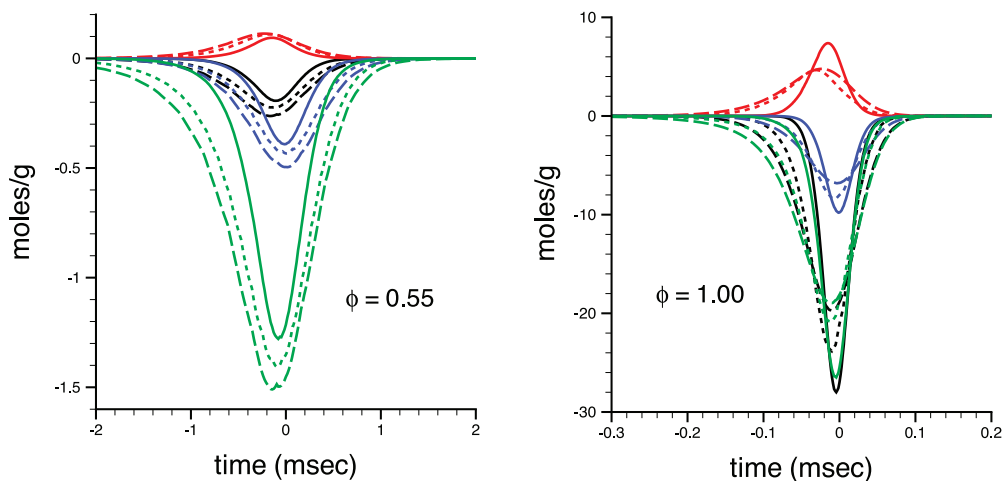
Figure 5: Profiles of the key reactions along the pathlines. Here, Rx. 11 is blue, Rx. 52 is red, Rx. 53 is black and Rx. 98 is green. The solid lines are the cusps, the long dashes are the noses and the short dashes are the laminar flame.

methane. Thus, in each case, Rx. 11, 53, and 98 are always net methane destructors while Rx. 52 creates methane. There is, however, some shift in the relative importance of the different reactions with equivalence ratio reflecting a change in the balance of the chemical pathways. For $\phi = 1.00$, Rx.'s 53 and 98 are essentially of equal importance with Rx.'s 11 and 52 playing a considerably less important role. Therefore, methane molecules are more often attacked by H and OH radicals than by O, and third-body-assisted recombination plays a reduced role. For the lean case, the OH radical plays the dominant role in the destruction of methane.

Figure 5 shows that for both $\phi = 0.55$ and $\phi = 1.00$, the reaction profiles through the nose are broader than those through the cusp. This reflects the notion that in a Lagrangian sense, the passage of fluid through the noses occurs on a slower time scale than through the cusps. However, in the $\phi = 1.00$ case, the reactions at the cusp reach higher intensities than those at the nose while for $\phi = 0.55$ the reactions in the nose are not only of longer duration but also reach higher intensities.

Fig. 6 shows the detailed decomposition of the pathlines for the three key radicals and methane, showing the diffusive transport and reaction components of each parcel's evolution. We see that, in both cases, the diffusion of methane out of the preheat zone is enhanced in the cusps, which represents a defocusing associated with transport of methane to nearby flame segments. For the lean case, this loss of fuel is reflected in an overall reduction in the radical pool and a subsequent reduction in the intensity of the methane oxidation; see Figure 4 (right).

For the $\phi = 1.00$ case the situation is somewhat different. Here, the peak production of H in the nose and the cusp are comparable, as is the subsequent transport of H out of that region. However, on the cooler side of the flame we see a dramatic increase in
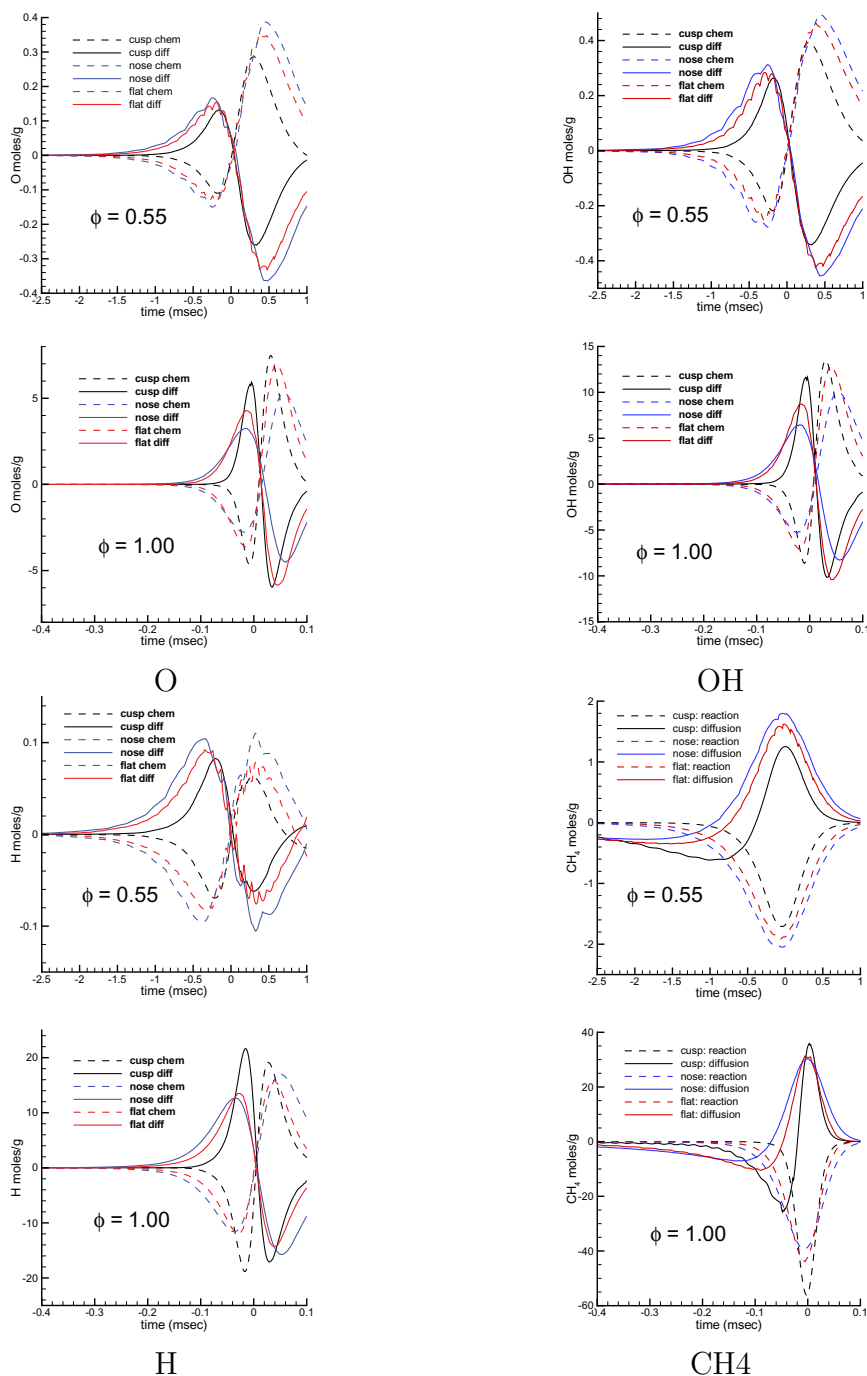
Figure 6: Decomposition of changes of O, OH, H, and CH_4 along the pathline. In each case, the solid lines represent diffusion and dashed lines represent reactions.

the peak diffusive flux of H onto the pathline. (A similar but less severe effect is also seen in O and OH.) This represents a diffusive focussing of highly mobile H radicals

(and to a lesser degree O and OH) from nearby flame segments into this parcel of fluid. This enhanced radical pool more than compensates for the decreased consumption of methane that results from diffusive defocusing toward the flame surface. At the nose, we see a modest focussing of CH_4 diffusion onto the pathline that leads to a net increase in the total amount of fuel consumed along the pathline. However, at the nose the fluid approaches the flame more slowly and spends more time in the flame zone. The fluid is heated more slowly and the key reactions act over longer periods of time at reduced temperatures and, consequently, lower rates. We see a corresponding net reduction of the peak of each of the key methane reactions. Although the peaks are low, the total amount of methane destroyed by each of the reactions (numbers 11, 53, and 98) increases, when integrated over the entire pathline.

The response of both flames to curvature has been shown here to be the result of a balance between competing effects. In both flames, the fuel molecules approaching the flame are diffused off pathlines in cusped regions and onto pathlines in nose regions. By removing fuel from the pathline in cusps, there are less fuel atoms to ultimately generate radicals. Conversely, the flux of radicals, which in both cases oppose that of the approaching fuel, are defocused in nose regions and focused in cusp regions. This has the effect of increasing the rate at which the fuel atoms are attacked in the cusps. Classical flame theory predicts that in the special (non-physical) case that the fuel and all radicals have identical mobilities, these effects balance each other in such a way that the Eulerian measure of fuel consumption rate becomes identically independent of flame curvature. However, hydrogen atoms are considerably more mobile than all other species, and the resulting competition therefore is strongly dependent on the extent to which hydrogen plays a role in fuel consumption. Our pathline analysis shows that a significant fraction of the the fuel atoms in the stoichiometric flame are attacked by hydrogen, so that when the hydrogen flux is focused by flame curvature, the resulting fuel consumption rate shows a net increase. The lean flame shows a far weaker dependence on hydrogen attack, and, as a result is far less affected by the increase in the flux divergence of hydrogen atoms, and rather more sensitive to preferential loss of fuel atoms. Moreover, the longer residence times and focusing of fuel in the noses results for the lean flame in enhanced fuel consumption, in spite of the increased hydrogen losses due to the defocusing of radicals.

In more qualitative[28] or simplified settings,[22] variations in combustion chemistry driven by the preferential diffusion of various fuel species have been categorized in terms of a fuel-based Lewis number (dimensionless ratio of heat to mass diffusivities). In order to more closely connect the present work to the existing literature on the subject, we are tempted to define our cases in terms of suitably-defined Lewis numbers. However, as discussed in the references[22] and the citations therein, the definition of a single mixture Lewis number is problematic–a different Lewis number can be defined for each species, and each of these will be spatially non-uniform. Moreover, the Lewis number most relevant to discussions of simplified chemistry is typically defined in terms of the *deficient* fuel species, which changes discontinously near $\phi = 1$. For finite-thickness flames computed

here using detailed chemistry and tranport, the simplified cartoon of the combustion process afforded by the Lewis number concept is not particularly useful or applicable.

5 CONCLUSIONS

We have introduced a pathline diagnostic that allows us to computationally follow parcels of fluid through the numerical computations of multi-dimensional reacting flow problems. Two turbulent premixed methane flames were studied with this pathline diagnostic to quantify precisely how preferential diffusion effects couple to geometrical perturbations in the flame surface. The flame surface was modulated by velocity perturbations in the premixed fuel stream designed to approximate turbulence, with length and velocity scales so that the resulting flames were in the identical corrugated/wrinkled flamelet turbulence/chemistry interaction regime. The flame solutions studied here were modeled using the GRI-Mech 3.0 specification for chemical kinetics and detailed transport, and evolved using a low Mach number projection algorithm with adaptive mesh refinement, coupled to a dynamic control strategy. The control algorithm produced fluctuating flames that were quasi-stationary in the domain.

In agreement with experimental data, we find that the correlation of the local rate of fuel-consumption with flame surface curvature changes sign as the equivalence ratio is changed from $\phi = 0.55$ to $\phi = 1.00$. The simulation data shows that the local flame speed is well-correlated with the curvature but is basically uncorrelated with instantaneous measures of the cold tangential strain rate.

The details of this change in fuel consumption were investigated with our new pathline analysis. We showed that for the lean case, defocusing of the fuel at cusped regions leads to a reduction in the combustion intensity. In the stoichiometric flame an intense focussing of radicals, particularly H, into the fuel premixtures enhances the combustion process and more than compensates for losses of methane to diffusion. In both the lean and stoichiometric cases, preferential diffusion results in a complex balance of effects in such a way that sign of the Markstein number for the fuel is strongly dependent on the composition of the radical pool instrumental in the attack of the fuel; in turn, this composition is highly dependent on the premixed fuel stoichiometry.

The pathline approach to data interrogation extends naturally to three dimensional data sets. Also, a statistical approach to data collection would allow a more systematic analysis of two and three dimensional data. Both suggestions are under current development for use in the analysis of these flames, and more complex scenarios. Finally, it is well-known that flow field strain has significant effect on the detailed chemistry of steady hydrocarbon flames. Flow strain will modify local residence times of the fuel while under attack from the radical pool, which as we have shown, will be strongly dependent on flame geometry and fuel composition. However, it is evident that the relationship of strain to fuel consumption has a temporal correlation that is not immediately discernable in the *instantaneous* diagnostics. In contrast, curvature of the flame surface was shown to be directly correlated to the instantaneous chemistry. This suggests that curvature

and flow strain, classically combined into a single "stretch" effect, in fact operate on disparate length and/or time scales. The pathline tool would appear to provide a natural framework with which we can quantitatively investigate the temporal correlation of strain and curvature effects, allowing a more complete distinction of effects of the two on flame chemistry. These investigations are the subject on ongoing research.

6   ACKNOWLEDGMENTS

REFERENCES

[1] N. Peters. *Turbulent Combustion*. Cambridge University Press, Cambridge, 2000.

[2] L.-K. Tseng, M. A. Ismail, and G. M. Faeth. Laminar burning velocities and Markstein numbers of hydrocarbon / air flames. *Combust. Flame*, 95:410–425, 1993.

[3] J. H. Chen and H. Im. Correlation of flame speed with stretch in turbulent premixed methane/air flames. *Proc. Combust. Inst.*, 27:819–826, 1998.

[4] J. B. Bell, M. S. Day, J. F. Grcar, and M. J. Lijewski. Active control for statistically stationary turbulent premixed flame simulations. *Comm. App. Math. Comput. Sci.*, 1:29–52, 2006.

[5] S. B. Pope, P. K. Yeung, and S. S. Girimaji. The curvature of material surfaces in isotropic turbulence. *Phys. Fluids A*, 1:2010–2018, 1989.

[6] C. J. Rutland and A. Trouvé. Direct simulations of premixed turbulent flames with non-unit Lewis numbers. *Combust. Flame*, 94:41–57, 1993.

[7] M. Baum, T. J. Poinsot, D. C. Haworth, and N. Darabiha. Direct numerical simulation of $H_2/O_2/N_2$ flames with complex chemistry in two-dimensional turbulent flows. *J. Fluid Mech.*, 281:1–32, 1994.

[8] D. C. Haworth, R. J. Blint, B. Cuenot, and T. J. Poinsot. Numerical simulation of turbulent propane-air combustion with nonhomogeneous reactants. *Combust. Flame*, 121:395–417, 2000.

[9] A. Trouvé and T. J. Poinsot. The evolution equation for the flame surface density in turbulent premixed combustion. *J. Fluid Mech.*, 278:1–31, 1994.

[10] S. Zhang and C. J. Rutland. Premixed flame effects on turbulence and pressure-related terms. *Combust. Flame*, 102:447–461, 1995.

[11] N. Chakraborty and S. Cant. Unsteady effects of strain rate and curvature on turbulent premixed flames in an inflow outflow configuration. *Combust. Flame*, 137:129–147, 2004.

[12] M. Tanahashi, M. Fujimura, and T. Miyauchi. Coherent fine scale eddies in turbulent premixed flames. *Proc. Combust. Inst.*, 28:529–535, 2000.

[13] M. Tanahashi, Y. Nada, Y. Ito, and T. Miyauchi. Local flame structure in the well-stirred reactor regime. *Proc. Combust. Inst.*, 29:2041–2049, 2002.

[14] J. B. Bell, M. S. Day, and J. F. Grcar. Numerical simulation of premixed turbulent methane combustion. *Proc. Combust. Inst.*, 29:1987–1993, 2002.

[15] M. S. Day and J. B. Bell. Numerical simulation of laminar reacting flows with complex chemistry. *Combust. Theory Modelling*, 4:535–556, 2000.

[16] J. B. Bell, M. S. Day, I. G. Shepherd, M. Johnson, R. K. Cheng, J. F. Grcar, V. E. Beckner, and M. J. Lijewski. Numerical simulation of a laboratory-scale turbulent V-flame. *Proc. Natl. Acad. Sci. USA*, 102(29):10006–10011, 2005.

[17] J. B. Bell, M. S. Day, J. F. Grcar, M. J. Lijewski, J. F. Driscoll, and S. A. Filatyev. Numerical simulation of a laboratory-scale turbulent slot flame. *Proc. Combust. Inst.*, 31, 2006. to appear.

[18] J. B. Bell, M. S. Day, R. K. Cheng, and I. G. Shepherd. Numerical simulation of lewis number effects on lean premixed turbulent flames. *Proc. Combust. Inst.*, 31, 2006. to appear.

[19] R. J. Kee, J. F. Grcar, M. D. Smooke, and J. A. Miller. PREMIX: A fortran program for modeling steady, laminar, one-dimensional premixed flames. Technical Report SAND85-8240, Sandia National Laboratories, Livermore, 1983.

[20] D. Bradley, P. H. Gaskell, and X. J. Gu. Burning velocities, Markstein lengths, and flame quenching for spherical methane-air flames: A computational study. *Combust. Flame*, 104:176–198, 1996.

[21] S. B. Pope. The evolution of surfaces in turbulence. *Int. J. Engng. Sci.*, 26:445–469, 1988.

[22] D. C. Haworth and T. J. Poinsot. Numerical simulations of Lewis number effects in turbulent premixed flames. *J. Fluid Mech.*, 244:405–436, 1992.

[23] T. Poinsot and D. Veynante. *Theoretical and Numerical Combustion.* R. T. Edwards, Inc., Philadelphia, 2001.

[24] S. H. Chung and C. K. Law. An integral analysis of the structure and propagation of stretched premixed flames. *Combust. Flame*, 72:325–336, 1988.

[25] L. P. H. de Goey and J. H. M. ten Thije Boonkkamp. A mass-based definition of flame stretch for flames with fine thickness. *Combustion Science and Technology*, 122:399–405, 1997.

[26] L. P. H. de Goey, R. M. M. Mallens, and J. H. M. ten Thije Boonkkamp. An evaluation of different contributions to flame stretch for stationary premixed flames. *Combust. Flame*, 110:54–66, 1997.

[27] L. P. H. de Goey and J. H. M. ten Thije Boonkkamp. A flamelet description of premixed laminar flames and the relation with flame stretch. *Combust. Flame*, 119:253–271, 1999.

[28] F. A. Williams. *Combustion Theory.* Addison-Wesley, Menlo Park, 2nd edition, 1988.